nature photonics

ARTICLES

https://doi.org/10.1038/s41566-021-00819-6

Mid-infrared semimetal polarization detectors with configurable polarity transition

Jingxuan Wei[1,2], Cheng Xu[1,2], Bowei Dong[1,2], Cheng-Wei Qiu[1]✉ and Chengkuo Lee[1,2]✉

On-chip polarization-sensitive photodetectors offer unique opportunities for next-generation ultra-compact polarimeters. So far, mainstream approaches have relied on the anisotropic absorption of natural materials or artificial structures. However, such a model is inherently restricted by correlation between the polarization ratio (PR) and diattenuation, leading to small PR values ($1 < PR < 10$). Here, we report nanoantenna-mediated semimetal photodetectors, which enable configurable polarity transition by exploiting the vectorial and non-local photoresponse in semimetals. By tuning the orientation of nanoantennas, PR values vary from positive (unipolar regime) to negative (bipolar regime), covering all possible numbers ($1 \rightarrow \infty/-\infty \rightarrow -1$). In particular, the PR values at the polarity-transition point could approach infinity. Such a polarity transition hereby transcends the conventional PR–diattenuation relationship. Furthermore, our device allows the subtle measurement of polarization-angle perturbation down to 0.02° $Hz^{-1/2}$ in the mid-infrared range. Our findings highlight the potential of semimetals as a promising material platform for miniaturized polarimetry.

Polarization, as an intrinsic attribute of light, plays a critical role in almost all optics-related phenomena and technologies, including imaging, remote sensing and navigation[1,2]. However, fine polarization scrutinization remains tricky and usually requires bulky polarization optics because traditional cameras are only sensitive to light intensity[3–5]. Specifically, three main approaches have been developed for polarization cameras. (1) 'Division-of-time': images of different polarization states are acquired sequentially in time[3]. The inherent drawbacks of this approach include limited temporal resolution, complicated design and high cost. (2) 'Division-of-amplitude': light is split by a set of polarization optics and delivered into separate detectors[1,6]. Although this approach allows for the concurrent detection of multiple polarization states, it natively requires a large propagation space to separate the split light and achieve accurate registration. (3) 'Division-of-focal-plane': a photodetector array is placed at the imaging focal plane and covered with wire-grid micropolarizers[7,8]. Despite its successful commercialization, this approach cannot provide measurement of full-Stokes parameters and subwavelength detection of structured beams.

In addition to the aforementioned three approaches, on-chip polarization-sensitive photodetectors have recently emerged as a promising candidate for polarization detection, enabling advanced polarization cameras[9–11]. Thanks to the filterless flat configuration, such functional photodetectors do not suffer from pixel cross-talk and can be smaller than the wavelength of light[12], making them capable of polarization imaging with ultra-high pixel density. Besides, this kind of photodetector has been reported to detect the linear polarization[9,10], circular polarization[13] and even the orbital angular momentum of light[14], resulting in the measurement of full-Stokes or even generalized Stokes parameters[15]. Studies on polarization-sensitive photodetectors could date back to solution-processed one-dimensional nanowires two decades ago[16–18]. Recently, we have seen a new surge of interest in this field, primarily due to the rediscovery of anisotropic two-dimensional (2D) materials that are compatible with the complementary metal-oxide–semiconductor (or CMOS) technology[10,11,19–22]. One crucial figure of merit to characterize polarization-sensitive photodetectors is the PR[23,24], which may also be differently defined as the extinction ratio[7,10], contrast ratio[9], polarization sensitivity[25,26] or anisotropic ratio[11,21]. To avoid potential confusion[16], we define the PR in this work as the ratio of maximum and minimum polarization-dependent photoresponse, and $|PR| > 1$. In practice, PR values are desired to be higher than 20 (ref. [7]). However, the PRs of 2D materials are generally below ten, although a large PR (of >100) was once reported in black phosphorus at a wavelength of 3.5 μm (Fig. 1a). Such small PRs result from an inherent correlation between the PR and anisotropic absorption (also known as linear dichroism or diattenuation)[11,19,27]. Although diattenuation engineering has been the mainstream method for polarization-sensitive photodetectors, the realization of large PRs is challenging. On the other hand, we draw attention to a less noticed zero-bias photoresponse in materials with broken centrosymmetry, such as ferroelectrics, where the flow direction of photo-carriers can be flipped by the polarization angle of light[28–30]. In contrast to conventional materials, the PR in such materials would be negative by definition. In the following, we term the two distinct types of polarization dependence as unipolar ($PR \geq 1$) and bipolar ($PR \leq -1$), where the photocurrents are sign-maintaining and sign-flipping, respectively. Efficiently implementing these two distinct phenomena within one chip-level platform may bring many unprecedented opportunities such as gigantic PR, but that has remained elusive[31].

Here, we demonstrate nanoantenna-mediated few-layer graphene photodetectors, yielding a configurable transition between unipolar and bipolar polarization dependence and providing full coverage of PR values from 1 to $\infty/-\infty$ then to -1 (Fig. 1a). Our device consists of periodically oriented metallic nanoantennas on a graphene transistor and works at zero drain–source bias under uniform illumination (Fig. 1b). By controlling the orientation angles of the nanoantennas (θ_1, θ_2), the PRs of our device can vary from positive to negative values (Fig. 1c,d). At the polarity-transition points, the PRs increase to infinity. The polarity transition is also illustrated in the measured iso-photoresponse contours, which change from

[1]Department of Electrical and Computer Engineering, National University of Singapore, Singapore, Singapore. [2]Center for Intelligent Sensors and MEMS, National University of Singapore, Singapore, Singapore. ✉e-mail: chengwei.qiu@nus.edu.sg; elelc@nus.edu.sg

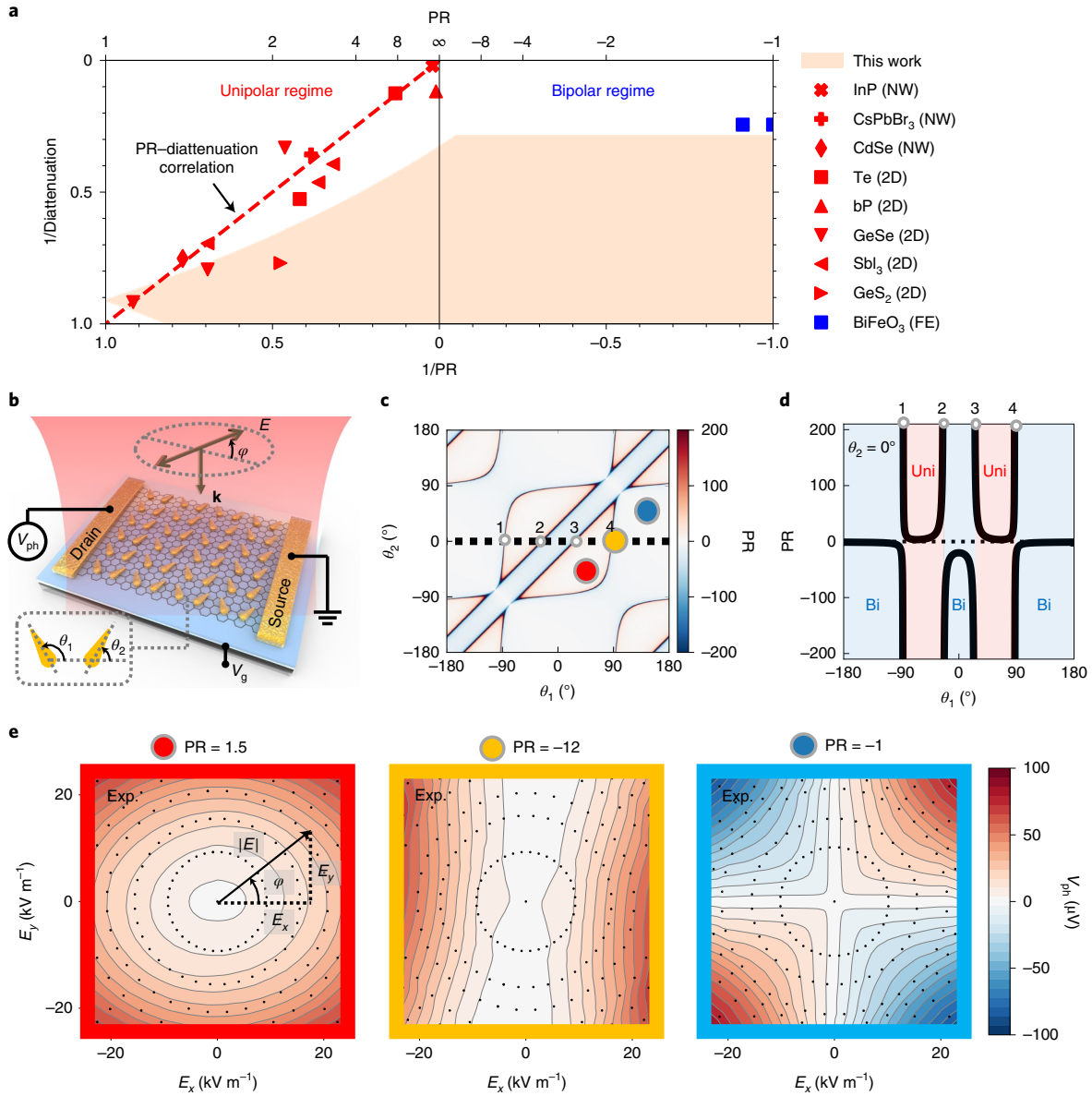

Fig. 1 | Design principles and main results of our designed nanoantenna-mediated semimetal photodetectors. a, Comparison of polarization-sensitive photodetectors. The photoresponse PR of a material is plotted against its diattenuation, showing two distinct regimes: unipolar (PR > 0) and bipolar (PR < 0). Data are taken from the literature (InP (ref. [16]), $CsPbBr_3$ (ref. [18]), CdSe (ref. [17]), Te (ref. [11]), bP (ref. [10]), GeSe (ref. [20]), SbI_3 (ref. [19]), GeS_2 (ref. [22]) and $BiFeO_3$ (ref. [28])). bP, black phosphorus; NW, nanowire; 2D, two-dimensional material; FE, ferroelectric. **b**, Schematic of the designed nanoantenna-mediated semimetal photodetector which consists of an array of metallic nanoantennas on a graphene transistor. From bottom to top: silicon (dark grey), SiO_2 (blue), graphene (black honeycomb) and nanoantennas and electrodes (yellow). The unit cell of the array is a pair of tapered nanoantennas with different orientation angles, θ_1 and θ_2; **k** denotes the wave vector of the incident light; E and φ represent the magnitude and polarization angle of the electric field of the light, respectively, and V_g is the gate voltage. The photovoltage, V_{ph}, values are measured in an open circuit. **c**, Calculated PRs as a mapping of (θ_1, θ_2) values. Note that |PR| is >1 by definition. **d**, Cutline plot of the PRs along the dashed line in **c**. The unipolar (Uni) and bipolar (Bi) regimes are shaded red and blue, respectively. The numbers 1, 2, 3 and 4 label the polarity-transition points where the PR values increase to infinity. **e**, Measured (Exp.) photovoltage at different incident power ($\propto |E|^2$) and φ. The wavelength of incident light is 4 μm. To illustrate the data, we have used the projected components of E for the x and y axes: $E_x = |E|\cos\varphi$ and $E_y = |E|\sin\varphi$. The grey solid lines represent the fitted iso-photovoltage contours, which are closed in unipolar devices but open in bipolar devices. The (θ_1, θ_2) values of the three samples were (45°, −45°), (90°, 0°) and (135°, 45°), respectively, as marked by the red, yellow and blue circles in **c**.

closed ellipses to open hyperbolas (Fig. 1e). In addition to the geometrical configurability, the PRs are also electrically tunable by applying a gate voltage, V_g, if heterogeneous structures are used. Finally, we reveal the bipolar device as a self-contained balanced photodetector, with a measured noise-equivalent polarization-angle perturbation down to 0.02° $Hz^{-1/2}$ in the mid-infrared range where high-performance miniaturized detectors remain challenging to be realized.

Results

Principle and mechanism. The microscopic origin of the photoresponse in our device can be attributed to the local photocurrents

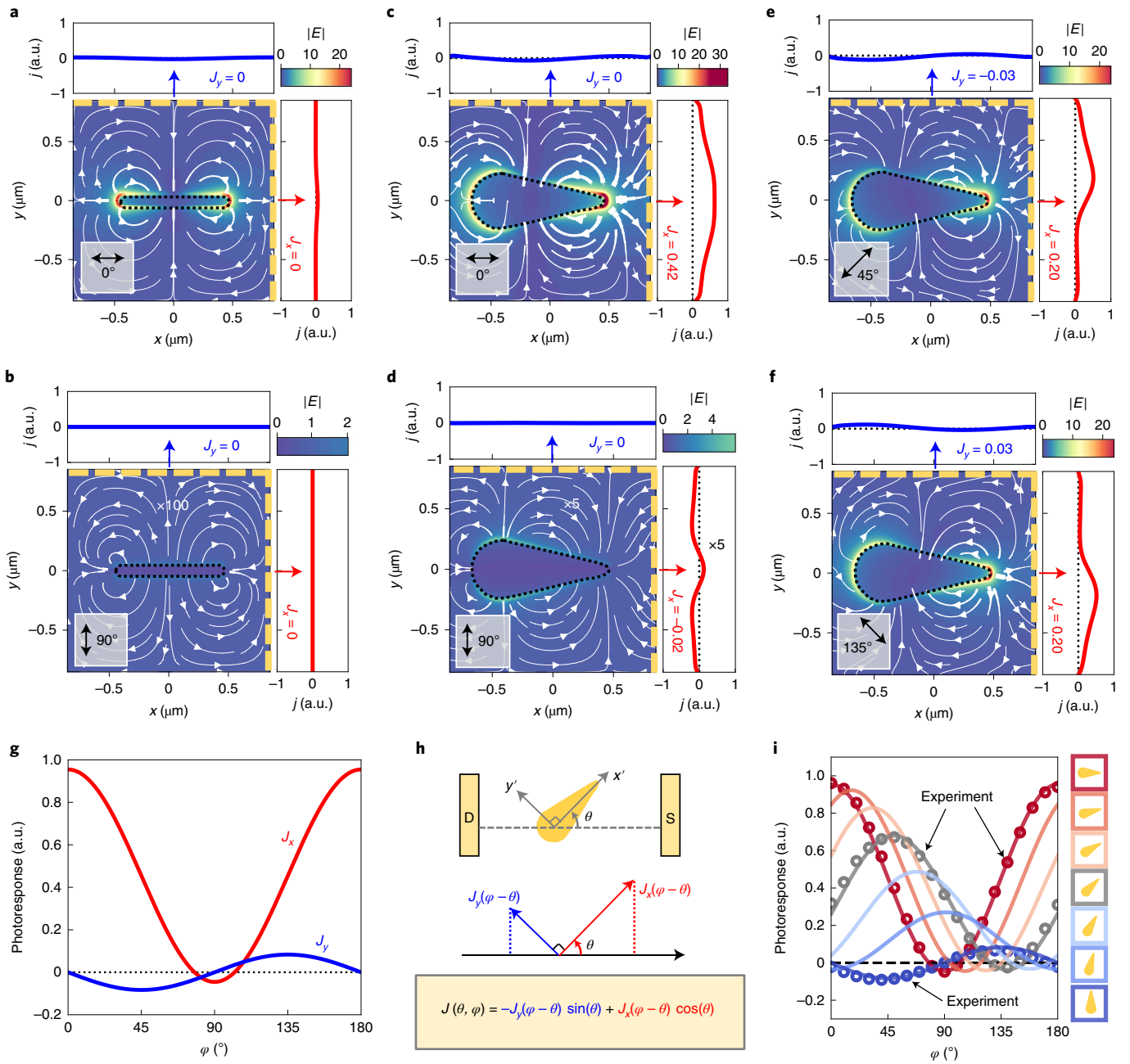

Fig. 2 | Polarization- and orientation-dependent photoresponse in tapered nanoantennas on graphene. a,**b**, Simulated photoresponse of untapered nanoantennas at 0° (**a**) and 90° (**b**) polarization of incident light. The overall photoresponse is symmetry forbidden and is always zero. Periodic boundary conditions are used in the modelling. White streamlines indicate the flow of carriers in graphene. J_x and J_y denote the normalized photocurrents flowing along the *x* and *y* directions, respectively. *j* represents the projected component of current density. **c**–**f**, Simulated photoresponse of 0°-oriented tapered nanoantennas at 0° (**c**), 90° (**d**), 45° (**e**) and 135° (**f**) polarization. The broken centrosymmetry allows for unbalanced photoresponse at zero external bias. **g**, Plot of J_x and J_y against φ. **h**, Illustration of the photoresponse calculation for tapered nanoantennas with an orientation angle of θ via coordinate transformation. Parameters *x*′ and *y*′ represent the nanoantenna coordinates. Drain (D) and source (S) electrodes are placed horizontally in laboratory coordinates. $J(\theta, \varphi)$ is the polarization and orientation-dependent photoresponse that can be collected by an external circuit. **i**, Calculated (lines) and measured (symbols) photoresponse of nanoantennas with θ ranging from 0° (red) to 90° (blue).

generated at the metallic nanoantennas–graphene interfaces[32,33]. So far, hot carriers and the photo-thermoelectric effect have been widely accepted as the dominating mechanisms for graphene's photoresponse over the photovoltaic effect, from the visible to the mid-infrared wavelength range[34,35]. We measured similar gate-dependent photoresponses in our devices at 4 μm wavelength, which suggest the same mechanism (Supplementary Fig. 1). Besides, we note that intrinsic graphene plasmons are not likely to be excited at this wavelength[36], and the plasmons themselves do not contribute a d.c. photoresponse[37]. A more detailed discussion on the microscopic origin of photocurrents at metal–graphene interfaces is outside the scope of this manuscript. In the following, we explain our results in the framework of the hot-carrier mechanism. When graphene is deposited with metallic nanoantennas, it

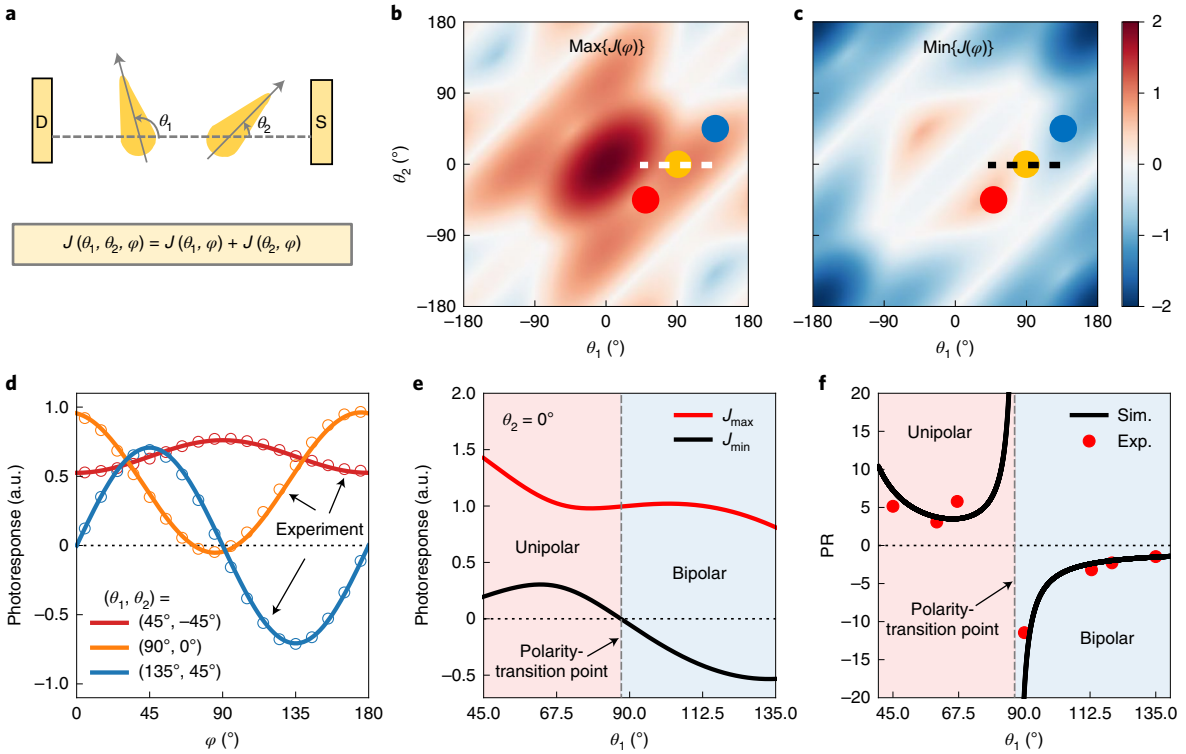

Fig. 3 | Geometrically tunable transition of polarization dependence. a, Calculation of the overall polarization-dependent photoresponse, $J(\theta_1, \theta_1, \varphi)$, after combining two types of tapered nanoantennas with orientation angles of θ_1 and θ_2. **b**,**c**, Calculation of the maxima (**b**) and minima (**c**) of $J(\theta_1, \theta_1, \varphi)$ with respect to φ. The colour bar shows the normalized photoresponse. **d**, Simulated (lines) and measured (symbols) photoresponse of three typical devices with their (θ_1, θ_2) values indicated by the filled circles in **b** and **c** with the same colours. **e**, Maxima and minima of the photoresponse along the cutline in **b** and **c**, indicating that a transition between unipolar and bipolar polarization dependence occurs around $(\theta_1, \theta_2) = (87°, 0°)$. The unipolar and bipolar regimes are shaded red and blue, respectively. **f**, Simulated (Sim.) and measured (Exp.) PRs along the cutline. The unipolar and bipolar regimes are shaded red and blue, respectively.

becomes doped[38] and hence its Seebeck coefficient is also tuned[39], forming a Seebeck gradient at the graphene–nanoantenna interfaces. Under the illumination, the incident light is concentrated at the edges of the nanoantennas due to plasmon localization[40]. As a result, hot carriers are excited with plasmonic enhancement and then driven by the Seebeck coefficient gradient to form local directional photocurrents[41].

The question then arises about how the hot carriers flow after that and whether or not the local photocurrents can be collected by the electrodes several micrometres away. At first glance, one might assume that the hot carriers with a picosecond-scale lifetime[42] should not diffuse a long distance before their recombination and hence do not contribute to the measured photocurrents. However, this concept has been challenged by many experiments showing that the locally excited photocurrents can be efficiently collected in a global manner[32,35,37,41]. Later, theoretical studies suggested that the local photocurrents can almost simultaneously establish an electric field throughout the gapless materials that drive the ambient carriers to contact electrodes, captured by a Shockley–Ramo-type framework[42]. We used few-layer graphene flakes in our experiments, which are semimetals[43,44], with the number of layer numbers between around three and eight (Supplementary Figs. 2–4). To simulate the global photoresponse in such a strongly correlated system, we should consider the collective behaviour of carriers in graphene and hence use hydrodynamic equations for the modelling[45,46] (see Supplementary Note 1 for more detailed discussions)

$$\frac{\partial \mathbf{u}(\mathbf{r})}{\partial t} = -\gamma \mathbf{u}(\mathbf{r}) - (\mathbf{u}(\mathbf{r})\nabla)\mathbf{u}(\mathbf{r}) + \nu\nabla^2\mathbf{u}(\mathbf{r}) - \frac{1}{\rho}\nabla\phi(\mathbf{r}) + \mathbf{F}(\mathbf{r}) \quad (1)$$

where $\mathbf{u}(\mathbf{r})$ is the velocity of charge carriers, $\phi(\mathbf{r})$ is the electric potential in the 2D plane, γ represents the Ohmic damping factor, ν and ρ are the viscosity and density of electrons in graphene, respectively, and $\mathbf{F}(\mathbf{r})$ denotes the spatially distributed source term assumed to scale with the local photoresponse at the metal–graphene interfaces. At equilibrium where $\partial/\partial t = 0$, the driving force is balanced by the Ohmic damping of electrons or the friction of non-slip boundaries of the devices. For a given charge density in graphene, n, we can further derive the current density, $\mathbf{J}(\mathbf{r}) = \mathbf{u}(\mathbf{r})n$.

Tapered nanoantenna design. We turn to the geometric design of nanoantennas. Although the charge-flow process discussed above already allows us to calculate the polarization-dependent photoresponse for a given nanoantenna structure, it provides little insight into guidelines. This section starts our design from a phenomenological description of the zero-bias photoresponse in the non-centrosymmetric system based on spatial symmetry[47]. Moreover, we limit our discussion to linear polarization and write the electric field of incident light as $\mathbf{E} = E_x\mathbf{x} + E_y\mathbf{y}$ with E_x and E_y as real values. Under uniform illumination, the photoresponse in our planar device possesses two components, J_x and J_y, written as[47]

$$\begin{pmatrix} J_x \\ J_y \end{pmatrix} = \begin{pmatrix} \beta_{xxx} & \beta_{xyy} & \beta_{xxy} \\ \beta_{yxx} & \beta_{yyy} & \beta_{yxy} \end{pmatrix} \begin{pmatrix} E_x^2 \\ E_y^2 \\ 2E_xE_y \end{pmatrix} \quad (2)$$

where β_{xxx}, β_{yyy}, β_{xyy}, β_{yxx}, β_{xxy} and β_{yxy} denote the elements of the photoresponse tensor (see Supplementary Note 2 for the detailed derivation).

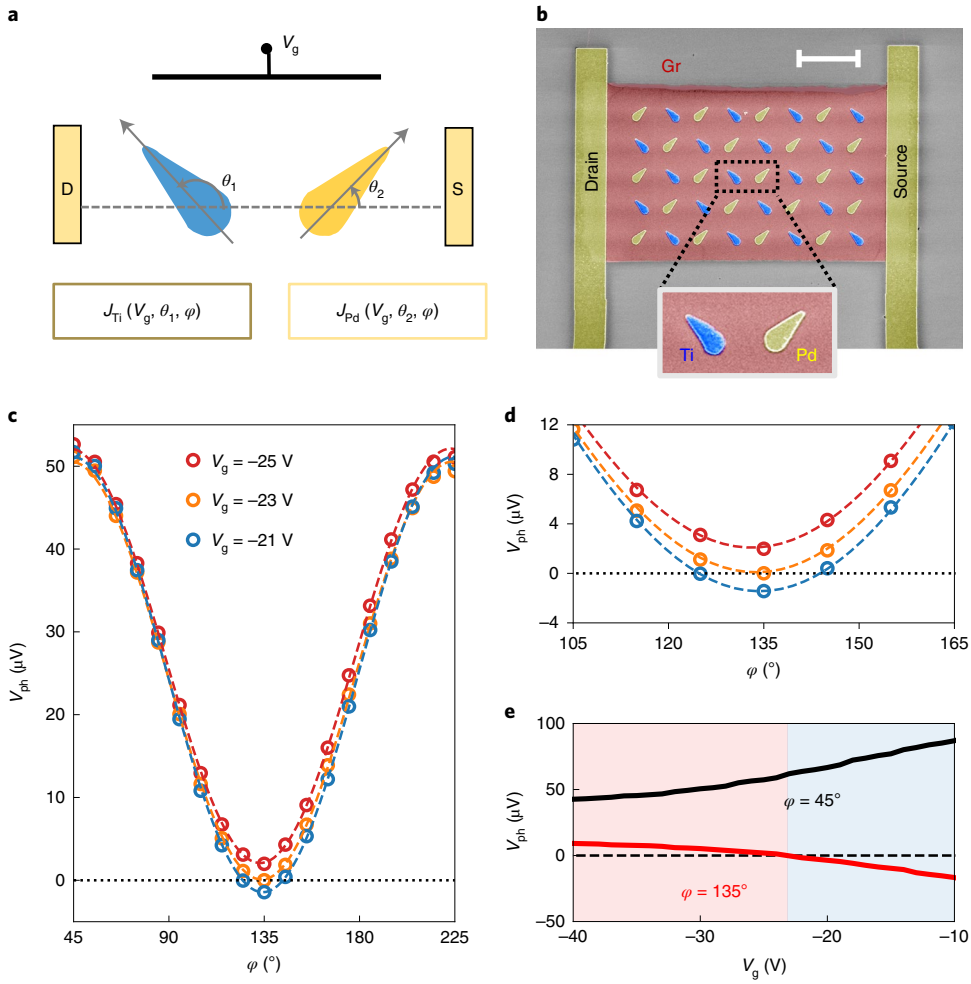

Fig. 4 | Electrically tunable transition of polarization dependence. a, Schematic of the heterogeneous structure of our device whose polarization dependence can be tuned by applying a gate voltage. J_{Ti} and J_{Pd} represent the photoresponse from gold nanoantennas with titanium and palladium adhesion layers, respectively. **b**, Scanning electron microscopy image of our device in false colours. Gr, graphene. Scale bar, 4 μm. **c**, Measured (symbols) and fitted (dashed lines) photovoltages versus φ at different gate voltages. **d**, Expanded plot of **c**. **e**, Measured gate-dependent photovoltages at $\varphi = 45$ and 135°, showing a transition of polarization dependence around $V_g = -23$ V. The red and blue shades indicate the unipolar and bipolar regimes, respectively. The corresponding PRs are from 4.7 ($V_g = -40$ V) to $\infty/-\infty$ ($V_g \approx -23$ V) then to −5.2 ($V_g = -10$ V).

The photoresponse tensor β is related to structural symmetry. In a centrosymmetric structure, β should remain the same after performing operations $x \rightarrow -x$ and $y \rightarrow -y$ in equation (2). This is only possible when all β values vanish. Our numerical simulation confirms this analysis with untapered nanorod antennas (Fig. 2a,b) in which the overall photoresponse is always negligible. To obtain an unbalanced photoresponse at zero bias, we must break the device centrosymmetry, for example by tapering the nanoantennas (Fig. 2c–f). A detailed relationship between the structure asymmetry and the unbalanced photoresponse is provided in Supplementary Fig. 7. In addition, the simulated polarization-dependent J_x and J_y allow us to extract the normalized β tensor:

$$\beta \approx \begin{pmatrix} 0.42 & -0.02 & 0 \\ 0 & 0 & -0.03 \end{pmatrix} \quad (3)$$

where the zeros in the tensor are simply due to the mirror symmetry with respect to the x axis.

Note that E_x and E_y are related to the amplitude $|E|$ and the polarization angle φ of the electric field: $E_x = |E|\cos\varphi$ and $E_y = |E|\sin\varphi$. Therefore, J_x and J_y are dependent on φ as $J_x \approx 0.42\cos^2\varphi - 0.02\sin^2\varphi$ and $J_y \approx -0.03\sin\varphi\cos\varphi$ (Fig. 2g). When the nanoantenna orientation is not along the drain–source direction, the resulting effective photocurrent summarizes the projected components of J_x and J_y (Fig. 2h), following a coordinate transformation (see Supplementary Note 3). Several examples for orientation angles θ, from 0 to 90° are shown in Fig. 2i (see Supplementary Fig. 8 for other angles).

We further experimentally validated the simulated polarization dependence with $\theta = 0$, 45 and 90°, respectively. The measured photovoltages have been rescaled in arbitrary units to compare with our simulation in Fig. 2i (see Supplementary Fig. 9 for original data and device images). Moreover, we characterized our device ($\theta = 0°$) in terms of I–V curves under dark and illuminated conditions, gate-dependent photovoltages, responsivity (15.6 V W^{-1}), dark noise spectra (down to 10 nV Hz$^{-1/2}$), noise-equivalent power (0.64 nW Hz$^{-1/2}$), wavelength dependence and response time (<667 ns) in Supplementary Figs. 10 and 11. The setup schematic is provided in Supplementary Fig. 12. In our experiments, the gate voltage is 0 V and the power density is 0.01 mW μm^{-2} unless noted otherwise. Finally, by scanning photovoltage measurements and frequency dependence studies, we conclude that the thermal effect does not play an important role in our device (Supplementary Note 4 and Supplementary Figs. 13–14).

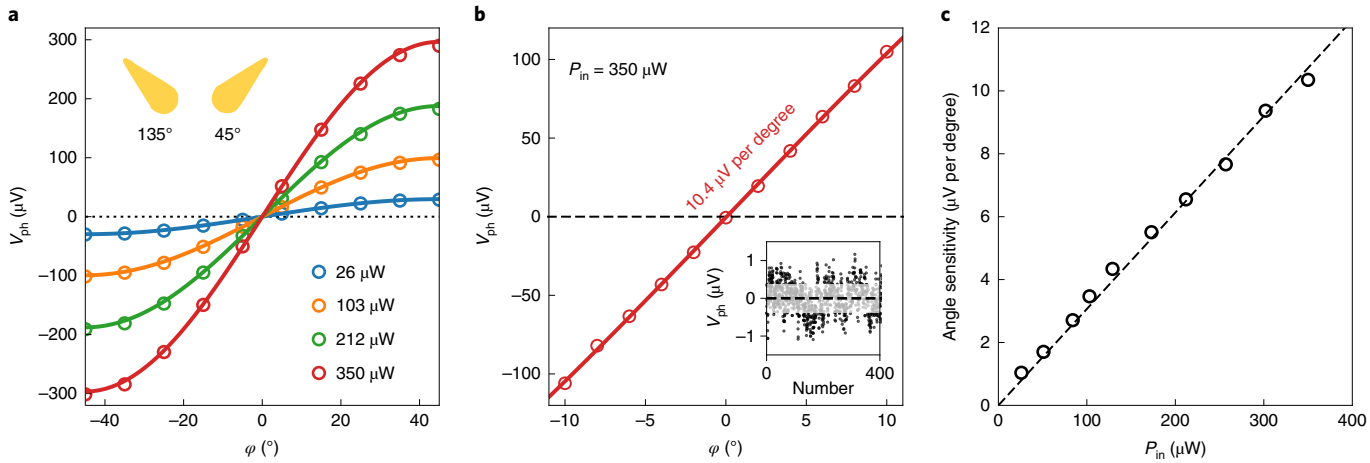

Fig. 5 | Measurement of small polarization-angle perturbation. a, Measured (symbols) polarization-dependent photovoltages, at different incident power levels, in a bipolar device with $(\theta_1, \theta_2) = (135°, 45°)$ and PR = −1. The inset shows the schematic of a unit cell. The results can be fitted well with the approximate sin(2φ) function, suggesting that this device can operate as a self-contained balanced polarization detector. One distinguishing feature in such a device is the non-vanishing polarization-angle sensitivity at $\varphi = 0°$ where the photoresponse approaches zero. The ability to work under such background-free conditions allows us to get rid of the effect of the laser intensity noise. **b**, Fine measurement of the polarization dependence, showing a polarization-angle sensitivity of 10.4 μV per degree at $\varphi = 0°$. The inset shows the measured voltage fluctuation, $\delta = 0.38$ μV, at a time constant of 0.1 s and hence an equivalent bandwidth of 2.5 Hz. Therefore, the detectivity of polarization-angle perturbation in our proof-of-concept device is 0.02° $Hz^{-1/2}$. **c**, Measured correlation between polarization-angle sensitivity and incident power, suggesting a large linear dynamic range.

Geometrically tunable transition of polarization dependence. Leveraging the orientation-controlled photoresponse in tapered nanoantennas, we design devices with a geometrically configurable transition between unipolar and bipolar polarization, by combining two types of nanoantennas with the respective orientation angles θ_1 and θ_2 (Fig. 3a). Our simulation confirms that near-field coupling between neighbouring nanoantennas should not be important (Supplementary Fig. 15). The maxima and minima of the polarization-dependent photoresponses for each set of (θ_1, θ_2) are calculated in Fig. 3b,c, from which we drive the geometrically configurable PRs (as we discussed in Fig. 1c). Owing to the breakdown of the PR–diattenuation correlation (see Supplementary Fig. 16 for the diattenuation calculation), the PRs in our device are switchable between the unipolar and bipolar regimes.

The geometrical configurability of the PR in our device is well exemplified in our fabricated devices with (θ_1, θ_2) = (45°, −45°), (90°, 0°) and (135°, 45°). In total, nine devices were fabricated, and we consistently observed contrasting PRs of about 1.5, −12 and −1 for the three types, respectively (see Supplementary Figs. 17 and 18). In Fig. 3d, we compare our simulation with the experimental results by adding an arbitrary scale factor, which shows a good agreement in the polarization dependence. Note that the relative orientation angle of the nanoantennas in those three designs are the same, namely, $\theta_1 - \theta_2 = 90°$; their diattenuation should also be the same value of unity, which is an excellent example of the broken PR–diattenuation correlation in our design.

We also investigated the robustness of the extremely large PR by sweeping θ_1 values from 45° to 135° with a fixed θ_2 at 0°. As shown in Fig. 3e, owing to the non-vanishing first derivative of photocurrent minimum J_{min}, the PRs will scale with $1/(\theta_1 - \theta_t)$ near the transition point ($\theta_t = 87°$). The reciprocal relationship indicates a fast drop of the PR when the parameters are away from the critical condition. The measured PR in our device with $\theta_1 = 90°$ (3° away from the transition point) was only about −12 (Fig. 3f).

Our proposed geometrically configurable PRs cover the full range, from 1 to ∞/−∞ then to −1. Specifically, a PR = 1 device with a completely polarization-insensitive photoresponse could be achieved around $(\theta_1, \theta_2) = (39°, -39°)$ or (141°, −141°) as shown in Supplementary Fig. 20. In addition, one example for a PR = ∞ device is at $(\theta_1, \theta_2) = (87°, 0°)$. Our simulated and experimental PR reaches above 100, limited by the accuracy of our measurement setup (Supplementary Figs. 21 and 22). Finally, PR = −1 devices have also been demonstrated as Fig. 3d.

Electrically tunable transition of polarization dependence. We further demonstrated an electrical-tuning approach via heterogeneous nanoantennas to achieve a configurable transition of polarization dependence, which may be useful in practice to compensate for fabrication errors (Fig. 4a). Here, we leverage the different gate dependence in two types of metal–graphene interfaces, such as titanium and palladium[48], to control the relative contribution of the photocurrents from differently oriented nanoantennas (see Supplementary Note 5 for detailed discussions). We fabricated Ti/Au and Pd/Au nanoantennas with respective orientation angles of 135 and 45° (Fig. 4b). A polarity transition was observed around $V_g = -23$ V (Fig. 4c). An expanded plot of the measured photovoltages near zero is illustrated in Fig. 4d. Furthermore, the electrical-tuning method is better illustrated in the measured gate-dependent photovoltages at polarization angles of 45 and 135°, corresponding to the maxima and minima (Fig. 4e). Extracted PRs are listed in Supplementary Table 2. When the photovoltages at $\varphi = 135°$ flip the sign around $V_g = -23$ V, the photovoltages at $\varphi = 45°$ remain large. The resulting PRs are huge (>100), limited by the accuracy of our setup. In practice, the technique of active-pixel sensors can be used to apply gate voltages for each device. Finally, we note that the gate-dependent photoresponse may drift over time, requiring passivation or encapsulation in practical applications (see Supplementary Fig. 24).

Measurement of small polarization-angle perturbation. To highlight the usefulness of our method, we reveal that the unusual bipolar device, with $(\theta_1, \theta_2) = (135°, 45°)$ and PR = −1, could be a self-contained balanced detector with great advantages for the measurement of small polarization-angle perturbation. Figure 5a illustrates the measured polarization-dependent photovoltages at different incident powers, all of which can be well fitted with the

function ~sin(2φ). Obviously, the integration of this function from $\varphi = 0$ to 180° is zero, indicating that the contribution of unpolarized light is inherently excluded in this device. In addition, because $\sin(2\varphi) = \cos^2(\varphi - 45°) - \cos^2(\varphi + 45°)$, the measured photovoltage directly reflects the differential intensity of polarization along two orthogonal directions, 45 and −45°.

As a feature of the balanced photodetection, our device shows the largest polarization-angle sensitivity at the point ($\varphi = 0°$) where the photoresponse vanishes. This background-free operation allows us to eliminate the laser intensity noise that is usually dominant in practical applications[49]. Our measurement also confirms the voltage noise at $\varphi = 45°$ under illumination to be 80% larger than *at* $\varphi = 0°$. Around the background-free point, we fine tuned the polarization angle and measured a polarization-angle sensitivity of 10.4 μV per degree and a noise density of 0.24 μV $Hz^{-1/2}$ at 350 μW illumination power, leading to a noise-equivalent polarization-angle rotation of about 0.02° $Hz^{-1/2}$ (Fig. 5b). This detectivity is comparable to the reported micropolarizer-filtered silicon detectors in the visible range[7], but our device operates in the mid-infrared region where the miniaturization of photodetectors remains tricky[50]. The measured noise at various illumination powers is provided in Supplementary Fig. 25. In addition, the measured power dependence of the polarization sensitivity indicates the extensive linear dynamic range of our device (Fig. 5c).

Discussion

Although we have limited our discussion to the detection of linearly polarized light in this work, our theoretical analysis and numerical designs can be readily extended to detect circularly polarized light (Supplementary Note 6 and Supplementary Fig. 26). Furthermore, the ability to implement both polarization-insensitive (PR = 1) and balanced (PR = −1) photodetectors allows us to measure the full-Stokes parameters directly. Since the geometric size of the nanoantenna is less than half the wavelength, a device with a single nanoantenna could enable the measurement of local polarization states in the subwavelength scale. We also note that our method is especially useful for infrared polarization imaging, where high-performance photodetection is still heavily dependent on bulky cryogenically cooled devices. What excites us most is that our theoretical analysis and numerical designs could, in principle, be extended to detect all the properties of light, including the intrinsic ones (intensity, wavelength, linear and circular polarization) and the extrinsic ones (angle of incidence and orbital angular momentum). Because these properties of light are correlated with the near field of specially designed nanoantennas, they can be detected by the proposed 2D semimetal photodetectors, which sense the near-field asymmetry of nanoantennas. A more detailed comparison with the existing nanoantenna-assisted 2D material photodetectors is provided in Supplementary Fig. 27 and Supplementary Table 3.

Looking forward, an improved model that correlates the incident power with the absolute photoresponse will be useful to optimize the structures further. The concurrent detection of intensity and polarization for certain specific applications would require multiple collaborative devices that acquire complementary information. Besides, exploring the setup-unlimited high-frequency photoresponse (>1 MHz) of our device in the mid-infrared range would be interesting. Furthermore, further studies on broadband polarization imaging via scrutinized antenna design would also be impactful. Last, we note that the concept of transition between unipolar and bipolar regimes is universal, which may also be implemented in other material systems, including the emerging topological materials and doped ferroelectrics[28,44].

In conclusion, we have numerically designed and experimentally studied nanoantenna-mediated few-layer graphene photodetectors with geometrically and electrically tunable polarity transition between unipolar and bipolar polarization dependence. The resulting PRs cover all the possible values from 1 to ∞/−∞ then to −1. The demonstrated ultrabroad tunable polarization dependence, large PRs at the transition point, versatility in design and self-contained balanced polarization detection of our approach highlight the potential of semimetals for next-generation ultra-compact polarimetry.

Online content

Any methods, additional references, Nature Research reporting summaries, source data, extended data, supplementary information, acknowledgements, peer review information; details of author contributions and competing interests; and statements of data and code availability are available at https://doi.org/10.1038/s41566-021-00819-6.

Received: 19 December 2020; Accepted: 19 April 2021;
Published online: 24 May 2021

References

1. Rubin, N. A. et al. Matrix Fourier optics enables a compact full-Stokes polarization camera. *Science* **365**, eaax1839 (2019).
2. Graydon, O. Global position by polarization. *Nat. Photonics* **12**, 318–318 (2018).
3. Tyo, J. S., Goldstein, D. L., Chenault, D. B. & Shaw, J. A. Review of passive imaging polarimetry for remote sensing applications. *Appl. Opt.* **45**, 5453–5469 (2006).
4. Martínez, A. Polarimetry enabled by nanophotonics. *Science* **362**, 750–751 (2018).
5. Lepetit, T. & Kanté, B. Simultaneous Stokes parameters. *Nat. Photonics* **9**, 709–710 (2015).
6. Pors, A., Nielsen, M. G. & Bozhevolnyi, S. I. Plasmonic metagratings for simultaneous determination of Stokes parameters. *Optica* **2**, 716–723 (2015).
7. Gruev, V., Perkins, R. & York, T. CCD polarization imaging sensor with aluminum nanowire optical filters. *Opt. Express* **18**, 19087–19094 (2010).
8. Maruyama, Y. et al. 3.2-MP back-illuminated polarization image sensor with four-directional air-gap wire grid and 2.5-μm pixels. *IEEE Trans. Electron Devices* **65**, 2544–2551 (2018).
9. Yuan, H. et al. Polarization-sensitive broadband photodetector using a black phosphorus vertical p–n junction. *Nat. Nanotechnol.* **10**, 707–713 (2015).
10. Bullock, J. et al. Polarization-resolved black phosphorus/molybdenum disulfide mid-wave infrared photodiodes with high detectivity at room temperature. *Nat. Photonics* **12**, 601–607 (2018).
11. Tong, L. et al. Stable mid-infrared polarization imaging based on quasi-2D tellurium at room temperature. *Nat. Commun.* **11**, 2308 (2020).
12. Guo, Q. et al. Efficient electrical detection of mid-infrared graphene plasmons at room temperature. *Nat. Mater.* **17**, 986–992 (2018).
13. Li, W. et al. Circularly polarized light detection with hot electrons in chiral plasmonic metamaterials. *Nat. Commun.* **6**, 8379 (2015).
14. Ji, Z. et al. Photocurrent detection of the orbital angular momentum of light. *Science* **368**, 763–767 (2020).
15. Afshinmanesh, F., White, J. S., Cai, W. & Brongersma, M. L. Measurement of the polarization state of light using an integrated plasmonic polarimeter. *Nanophotonics* **1**, 125–129 (2012).
16. Wang, J., Gudiksen, M. S., Duan, X., Cui, Y. & Lieber, C. M. Highly polarized photoluminescence and photodetection from single indium phosphide nanowires. *Science* **293**, 1455–1457 (2001).
17. Singh, A. et al. Polarization-sensitive nanowire photodetectors based on solution-synthesized CdSe quantum-wire solids. *Nano Lett.* **7**, 2999–3006 (2007).
18. Feng, J. et al. Crystallographically aligned perovskite structures for high-performance polarization-sensitive photodetectors. *Adv. Mater.* **29**, 1605993 (2017).
19. Xiao, M. et al. Symmetry-reduction enhanced polarization-sensitive photodetection in core–shell SbI_3/Sb_2O_3 van der Waals heterostructure. *Small* **16**, 1907172 (2020).
20. Wang, X. et al. Short-wave near-infrared linear dichroism of two-dimensional germanium selenide. *J. Am. Chem. Soc.* **139**, 14976–14982 (2017).
21. Hong, T. et al. Polarized photocurrent response in black phosphorus field-effect transistors. *Nanoscale* **6**, 8978–8983 (2014).
22. Yang, Y. et al. Polarization-sensitive ultraviolet photodetection of anisotropic 2D GeS_2. *Adv. Funct. Mater.* **29**, 1900411 (2019).
23. Peng, Y. et al. Exploiting the bulk photovoltaic effect in a 2D trilayered hybrid ferroelectric for highly sensitive polarized light detection. *Angew. Chem. Int. Ed.* **59**, 3933–3937 (2020).

24. Venuthurumilli, P. K., Ye, P. D. & Xu, X. Plasmonic resonance enhanced polarization-sensitive photodetection by black phosphorus in near infrared. *ACS Nano* **12**, 4861–4867 (2018).
25. Wu, D. et al. Highly polarization-sensitive, broadband, self-powered photodetector based on graphene/$PdSe_2$/germanium heterojunction. *ACS Nano* **13**, 9907–9917 (2019).
26. Zeng, L. et al. Multilayered $PdSe_2$/perovskite Schottky junction for fast, self-powered, polarization-sensitive, broadband photodetectors, and image sensor application. *Adv. Sci.* **6**, 1901134 (2019).
27. Pi, L. et al. Highly in-plane anisotropic 2D $PdSe_2$ for polarized photodetection with orientation selectivity. *Adv. Funct. Mater.* **31**, 2006774 (2020).
28. Kim, D. J. & Alexe, M. Bulk photovoltaic effect in monodomain $BiFeO_3$ thin films. *Appl. Phys. Lett.* **110**, 183902 (2017).
29. Bhatnagar, A., Roy Chaudhuri, A., Heon Kim, Y., Hesse, D. & Alexe, M. Role of domain walls in the abnormal photovoltaic effect in $BiFeO_3$. *Nat. Commun.* **4**, 2835 (2013).
30. Wei, J. et al. Zero-bias mid-infrared graphene photodetectors with bulk photoresponse and calibration-free polarization detection. *Nat. Commun.* **11**, 6404 (2020).
31. Freitag, M. et al. Photocurrent in graphene harnessed by tunable intrinsic plasmons. *Nat. Commun.* **4**, 1951 (2013).
32. Park, J., Ahn, Y. H. & Ruiz-Vargas, C. Imaging of photocurrent generation and collection in single-layer graphene. *Nano Lett.* **9**, 1742–1746 (2009).
33. Xia, F., Mueller, T., Lin, Y., Valdes-Garcia, A. & Avouris, P. Ultrafast graphene photodetector. *Nat. Nanotechnol.* **4**, 839–843 (2009).
34. Gabor, N. M. et al. Hot carrier-assisted intrinsic photoresponse in graphene. *Science* **334**, 648–652 (2011).
35. Woessner, A. et al. Near-field photocurrent nanoscopy on bare and encapsulated graphene. *Nat. Commun.* **7**, 10783 (2016).
36. Alonso-González, P. et al. Controlling graphene plasmons with resonant metal antennas and spatial conductivity patterns. *Science* **344**, 1369–1373 (2014).
37. Lundeberg, M. B. et al. Thermoelectric detection and imaging of propagating graphene plasmons. *Nat. Mater.* **16**, 204–207 (2017).
38. Giovannetti, G. et al. Doping graphene with metal contacts. *Phys. Rev. Lett.* **101**, 026803 (2008).
39. Zuev, Y. M., Chang, W. & Kim, P. Thermoelectric and magnetothermoelectric transport measurements of graphene. *Phys. Rev. Lett.* **102**, 096807 (2009).
40. Yao, Y. et al. High-responsivity mid-infrared graphene detectors with antenna-enhanced photocarrier generation and collection. *Nano Lett.* **14**, 3749–3754 (2014).
41. Wang, D. et al. Enhancing the graphene photocurrent using surface plasmons and a p-n junction. *Light Sci. Appl.* **9**, 126 (2020).
42. Song, J. C. W. & Levitov, L. S. Shockley-Ramo theorem and long-range photocurrent response in gapless materials. *Phys. Rev. B* **90**, 075415 (2014).
43. Latil, S. & Henrard, L. Charge carriers in few-layer graphene films. *Phys. Rev. Lett.* **97**, 036803 (2006).
44. Liu, J., Xia, F., Xiao, D., García de Abajo, F. J. & Sun, D. Semimetals for high-performance photodetection. *Nat. Mater.* **19**, 830–837 (2020).
45. Bandurin, D. A. et al. Negative local resistance caused by viscous electron backflow in graphene. *Science* **351**, 1055–1058 (2016).
46. Bandurin, D. A. et al. Fluidity onset in graphene. *Nat. Commun.* **9**, 4533 (2018).
47. Sturman, B. I. & Fridkin, V. M. *Photovoltaic and Photo-refractive Effects in Noncentrosymmetric Materials* Vol. 8 (CRC, 1992).
48. Mueller, T., Xia, F. & Avouris, P. Graphene photodetectors for high-speed optical communications. *Nat. Photonics* **4**, 297–301 (2010).
49. Tomberg, T., Muraviev, A., Ru, Q. & Vodopyanov, K. L. Background-free broadband absorption spectroscopy based on interferometric suppression with a sign-inverted waveform. *Optica* **6**, 147–151 (2019).
50. Zeng, L. et al. Van der Waals epitaxial growth of mosaic-like 2D platinum ditelluride layers for room-temperature mid-infrared photodetection up to 10.6 μm. *Adv. Mater.* **32**, 2004412 (2020).

Methods

Simulation. The optical responses of a 2D array of nanoantennas on graphene were simulated with a single unit and applying periodic boundary conditions, using the finite-difference time-domain method (FDTD Solutions package, Lumerical). The light source was a plane wave with normal incidence from the air. The boundaries above and below the array of nanoantennas were perfectly matched layers. Mesh spacings were below 10 nm in all dimensions. From bottom to top, the simulated structure consists of a silicon substrate, SiO_2 (300 nm thickness), graphene (2D surface-conductance model, no thickness), gold nanoantennas (60 nm thickness) and air. The absorption of graphene was calculated using the surface-conductance model. The modelling of nanoantenna-mediated current flow was implemented with our Python codes.

Device fabrication. The fabrication of our devices started from mechanically exfoliating few-layer graphene flakes from natural graphite (NGS Naturgraphit) onto a thermally oxidized (~285 nm) heavily p-doped silicon wafer, which served as a back gate. Metallic alignment markers (usually 3 nm titanium and 20 nm gold) were then fabricated using electron-beam lithography (EBL; JBX-6300FS, Jeol), thermal deposition and liftoff in acetone. With these alignment markers, we then patterned graphene to rectangles via a second round of EBL and oxygen plasma etching. The devices were then annealed at 350 °C for 6 h in an argon/hydrogen atmosphere to remove the resist residues. Thereafter, metallic nanoantennas and contacts were patterned on the graphene flakes by a third round of EBL and subsequent thermal deposition (5 nm palladium and 50 nm gold). Finally, a fourth round of EBL and thermal deposition (5 nm titanium and 60 nm gold) were used to pattern the titanium nanoantennas and larger electrodes for probing electrical characterization.

Characterization. Our measurements of photovoltages were conducted using a homemade optical system where the light from a quantum cascade laser (MIRCat-1200, Daylight Solutions) with high polarization purity (>100:1) was propagated in free space and delivered by uncoated mirrors onto the sample. A low-order half-wave plate (WPLH05M-4000, Thorlabs) designed at 4 μm was used to control the polarization angles of light. The photovoltages were measured using a lock-in amplifier (SR830, Stanford Research Systems) and the light signal was modulated using an optical chopper (SR540, Stanford Research Systems) at 1,368 Hz to get rid of the low-frequency noise and increase the signal-to-noise ratio. The equivalent bandwidth, B, can be set by the time constant, t: $B = 1/4t$. The low-frequency (<4 kHz) temporal response was measured using an oscilloscope with the signal pre-amplified (SR560, Stanford Research Systems). The high-frequency (>1 MHz) temporal response was characterized by the pulse mode of our nanosecond quantum cascade laser (MIRCat-1200) and calibrated using a commercial fast-speed mid-infrared photodetector (PDAVJ8—HgCdTe Amplified Photodetector, 100 MHz bandwidth, Thorlabs). The d.c. I–V curves at different gate voltages were measured using a semiconductor characterization system (4200-SCS, Keithley). The incident power was modulated by tuning the laser pump current and inserting neutral density filters (NDIR03A, NDIR10A, NDIR20A and NDIR30A, Thorlabs) and calibrated with a power meter (843-R, Newport).

Data availability

All technical details for producing the figures are enclosed in the Supplementary Information. Data are available from the corresponding authors C.-W.Q. or C.L. upon request.

Code availability

All technical details for implementing the simulation of nanoantenna-driven photocurrents in graphene are enclosed in the Supplementary Information. Python codes are available from the corresponding authors C.-W.Q. or C.L. upon request.

Acknowledgements

We thank Y. Li, G. Hu and X. Le for helpful discussions. This research was supported by the National Research Foundation Singapore (Grant No. NRF-CRP15-2015-02). C.-W.Q. acknowledges financial support from the National Research Foundation, Prime Minister's Office, Singapore under Competitive Research Program Award NRF-CRP22-2019-0006. C.-W.Q. is also supported by a grant (R-261-518-004-720) from Advanced Research and Technology Innovation Centre (ARTIC).

Author contributions

J.W., C.-W.Q. and C.L. conceived the project. J.W. did the theoretical analysis, numerical simulation and sample fabrication. J.W. carried out the device characterization with assistance from C.X. and B.D. All authors discussed the results. J.W., C.-W.Q. and C.L. wrote the manuscript with comments from all authors. C.-W.Q. and C.L. supervised the project.

Competing interests

The authors declare no competing interests.

Additional information

Supplementary information The online version contains supplementary material available at https://doi.org/10.1038/s41566-021-00819-6.

Correspondence and requests for materials should be addressed to C.-W.Q. or C.L.

Peer review information *Nature Photonics* thanks the anonymous reviewers for their contribution to the peer review of this work.

Reprints and permissions information is available at www.nature.com/reprints.